NOVEL TREE-LIKE WO_3 NANOPLATELETS WITH VERY HIGH SURFACE AREA SYNTHESIZED BY ANODIZATION UNDER CONTROLLED HYDRODYNAMIC CONDITIONS

Fernández-Domene, R.M.[a]; Sánchez-Tovar, R.[a]; Segura-Sanchís, E.[a]; García-Antón, J.[a]*

[a]*Ingeniería Electroquímica y Corrosión (IEC). Departamento de Ingeniería Química y Nuclear. ETSI Industriales. Universitat Politècnica de València. Camino de Vera s/n, 46022 Valencia, Spain.*

Tel. 34-96-387 76 32, Fax. 34-96-387 76 39, e-mail: jgarciaa@iqn.upv.es

In the present work, a new WO_3 nanostructure has been obtained by anodization in a H_2SO_4/NaF electrolyte under controlled hydrodynamic conditions using a Rotating Disc Electrode (RDE) configuration. Anodized samples were analyzed by means of Field Emission Scanning Electronic Microscopy (FE-SEM), Confocal Raman Microscopy and photoelectrochemical measurements. The new nanostructure, which consists of nanoplatelets clusters growing in a tree-like manner, presents a very high surface area exposed to the electrolyte, leading to an outstanding enhancement of its photoelectrochemical activity. Obtained results show that the size of nanostructures and the percentage of electrode surface covered by these nanostructures depend strongly on the rotation velocity and the electrolyte composition.

KEYWORDS: WO_3 nanostructures, acid electrolytes, anodization, hydrodynamic conditions, water splitting.

1. Introduction

Tungsten trioxide (WO_3) is an *n*-type semiconductor which has attracted considerable attention for the last decades due to its remarkable electrical, optical and structural properties and to its high resistance against photocorrosion in aqueous acidic solutions [1-9]. WO_3 has an ample range of applications: it has been widely used in electrochromic devices [10, 11], sensors [12-14], photoelectrochemical water splitting [4, 6, 7, 15-19], dye-sensitized solar cells [3, 5] and treatment of polluted aqueous systems using solar (or artificial) light [4, 7, 8, 20]. Nanostructured WO_3 layers have been developed to enhance the efficiencies of these processes, by increasing the surface area in contact with the electrolyte, enhancing effective light harvesting and reducing the charge transfer resistance [1, 3, 7, 8, 16, 21, 22].

Anodization of tungsten is a fast and simple method to synthesize WO_3 nanostructures [3, 4, 6, 9-13, 15, 19-25], in which surface morphology can be designed by adequately controlling several parameters, such as the anodization potential, duration, electrolyte composition and temperature, etc. [3, 9, 15, 25]. Moreover, WO_3 nanostructures formed by anodization can be grown directly on the substrate (the back metal collector), providing the basis for efficient charge collection.

In 2008, Widenkvist et al. [26] reported the formation of high surface area WO_3 nanostructures with a regular plate-like shape by immersing W samples in 1.5M HNO_3 at 50º C for 3 hours. This type of nanostructure has also been reported to form by immersing W in boiling 1.5M HNO_3 for several hours [27]. WO_3 nanoplatelets were also obtained by anodization at 20V for 4 hours in the same nitric acid electrolyte [3,

13]. A similar morphology (flower-like nanoplatelets) was produced by anodizing W at 50 V for 1 hour in a 1M H_2SO_4 electrolyte with 0.5 wt% NaF, at room temperature [9, 19]. An acidic treatment in 1M H_2SO_4 solution after anodizing W in 0.2 wt.% NH_4F aqueous solution also resulted in WO_3 nanoplatelets [28]. According to the literature, this type of nanostructure is formed in acid media by the precipitation of WO_4^{2-} to $WO_3 \cdot H_2O$ [26] or by the precipitation of WO_2^{2+} to $WO_3 \cdot 2H_2O$ [9, 28, 29], after reaching supersaturation conditions, with the soluble WO_4^{2-} and WO_2^{2+} ions being formed previously by dissolution of the substrate. In these works, it was also observed that when stirring the electrolyte during the reaction, the dimensions and/or morphology of the nanostructures changed, indicating the involvement of soluble species in their formation [9, 26]. However, no studies have been found dealing with WO_3 nanoplatelets growing under controlled hydrodynamic conditions, in which the mechanical convection of the solution near the electrode surface is reproducible, for example using a rotating disk electrode (RDE).

Recently we showed, anodizing Ti in glycerol/water electrolytes with fluoride ions and using a rotating electrode configuration, that under specific hydrodynamic conditions a transition from TiO_2 nanotubes to TiO_2 nanosponges took place [30]. Hence, the main goal of this study is to investigate the changes induced in the morphology of WO_3 nanostructures by altering, in a controlled way, the hydrodynamic conditions during anodization of W in H_2SO_4 electrolytes in the absence and presence of F^- ions, and the potential applications of the new obtained nanostructures for photoelectrochemical water splitting. WO_3 nanostructures were characterized by Field Emission Scanning Electronic Microscopy (FE-SEM), Confocal Raman Microscopy and photoelectrochemical measurements.

2. Experimental procedure

A Teflon coated tungsten rod (8 mm in diameter, 0.5 cm^2 of area exposed to the electrolyte) was used as a working electrode during anodization, and a platinum mesh as a counter electrode. Prior to anodization, tungsten surface was abraded with 220 to 4000 silicon carbide (SiC) papers, degreased by sonication in ethanol for 2 minutes and dried in a N_2 stream. A rotating electrode was used to perform anodization under controlled hydrodynamic conditions. Different rotation velocities were used: 0, 500 and 2000 rpm. Anodization was carried out in 1.5M H_2SO_4 solutions, without and with 0.1M NaF, at 20 V for 4 hours and at 50º C. Current densities were continuously measured during anodization. After anodization, the samples were annealed at 400º C for 4 hours in an air atmosphere.

The crystalline microstructure of WO_3 was examined by means of Confocal Raman Laser spectroscopy ("Witec Raman microscope"). For these measurements, a 632 nm neon laser with 420 μW was used. The morphology of the obtained nanostructures was characterized by using Field Emission Scanning Electron Microscopy (FE-SEM).

Photoelectrochemical water splitting tests were performed in an electrochemical cell with an Ag/AgCl 3M KCl reference electrode and a platinum tip counter electrode. The area of the WO_3 nanostructures (working electrode) exposed to the test solution was 0.13 cm^2 due to the electrochemical cell design. The photoelectrochemical measurements were conducted in a 0.1M H_2SO_4 solution using an Autolab PGSTAT302N potentiostat under simulated sunlight condition AM 1.5 (100 mW cm^{-2}). Photocurrent vs. potential curves were recorded by scanning the potential from −0.24

$V_{Ag/AgCl}$ to 1 $V_{Ag/AgCl}$ with a scan rate of 2 mV s^{-1}. Photocurrent transients as a function of the applied potential were recorded by chopped light irradiation (60 s in the dark and 20 s under illumination).

3. Results and discussion

3.1. Composition of the formed nanostructures.

Raman spectroscopy is a technique used to analyze the structure, phase and components of materials such as tungsten oxides, as well as to detect intercalated H_2O molecules in these oxides. **Figure 1** shows the Raman spectra of the as-anodized samples (**Figure 1a**) and after the heat treatment at 400º C for 4 h (**Figure 1b**). In the as-anodized samples, several common bands can be discerned. The band around 950-960 cm^1 is attributed to the symmetric stretching mode of a short terminal W^{6+}=O bond (ν_s(W=O)) [2, 3, 9, 14, 20, 27, 28, 31-34]; this terminal stretching is typical of dangling WO double bonds in weak interaction with water molecules, which are adsorbed at the free surface of internal grains and micro-void structures in the film, so it acts as a spectral marker for the amorphous $WO_3 \cdot n(H_2O)$ hydrated oxide [3, 9, 20, 32, 35-39]. The broad band between 600-700 cm^{-1} corresponds to the symmetric stretching vibrations of (O-W-O) bonds (ν_s(O-W-O) [2, 3, 28, 32]; in this case, since the band appears as a doublet (~660 cm^{-1} and ~680 cm^{-1}), the material can be identified as $WO_3 \cdot 2H_2O$ [2, 3, 9, 27]. The band between 190-280 cm^{-1}, where several peaks can be observed (at ~195 cm^{-1}, ~210 cm^{-1}, ~232 cm^{-1}, ~260 cm^{-1} and 270-280 cm^{-1}), is associated with the antisymmetric stretching vibration of (W-O-W) bonds (ν_a(W-O-W) [34]; concretely, the peaks around 195 cm^{-1} and 260 cm^{-1} indicate the presence of $WO_3 \cdot H_2O$ [34], the peaks at ~210 cm^{-1}

and ~270 cm^{-1} indicate the presence of $WO_3 \cdot 2H_2O$ [34], and the peak centered at ~ 235 cm^{-1} is related to the presence of both hydrous species [34]. On the other hand, the peak at ~810 cm^{-1} that appears clearly in the spectrum of the sample anodized at 2000 rpm without F^- (and to a lesser extent in the other samples) can be attributed to the existence of some crystalline monoclinic phase, with the feature at ~810 cm^{-1} being assigned to symmetric stretching vibrations of (O-W-O) bonds in the WO_6 octahedral units [8, 27, 32, 33]. These results, therefore, are indicative of amorphous $WO_3 \cdot 2H_2O$ with the presence of minor $WO_3 \cdot H_2O$ and some crystalline monoclinic phase.

The oxidation of W in a F^--free electrolyte takes place according to the following reaction [28, 40]:

$$W + 3H_2O \rightarrow WO_3 + 6H^+ + 6e^- \quad \textbf{(1)}$$

In acid solutions, WO_3 can undergo chemical dissolution, which is favored with increasing temperatures and results in the formation of cationic species such as WO_2^{2+} [9, 28, 29]:

$$WO_3 + 2H^+ \rightarrow WO_2^{2+} + 2H_2O \quad \textbf{(2)}$$

Subsequently, upon reaching supersaturation conditions, the soluble species WO_2^{2+} precipitates on the electrode surface, according to the following reactions [9, 28, 29]:

$$WO_2^{2+} + 3H_2O \rightarrow WO_3 \cdot 2H_2O + 2H^+ \quad \textbf{(3)}$$

$$WO_2^{2+} + 2H_2O \rightarrow WO_3 \cdot H_2O + 2H^+ \quad \textbf{(4)}$$

The relative kinetics of reactions (3) and (4) will determine the composition of the precipitate layer. According to the Raman spectra of the as-anodized samples discussed above, the main constituent of the hydrated WO_3 film is $WO_3 \cdot 2H_2O$, so under the present anodization conditions, reaction (3) is kinetically favored over reaction (4).

The Raman spectra of the anodized samples (**Figure 1b**) show different features. The band at around 950-960 cm^{-1} disappears and the broad band centered at ~660 cm^{-1} observed in the as-anodized spectra splits in two narrower bands, one centered at ~715 cm^{-2} and the other at ~806 cm^{-1}. Besides, three new peaks develop at ~190 cm^{-1}, ~276 cm^{-1} and ~330 cm^{-1}. This spectral change is related to the loss of water molecules by the oxide [38], and all the new peaks are typical of crystalline monoclinic WO_3: the strong peaks located at 806 and 715 cm^{-1} correspond to the symmetric stretching vibration of (O-W-O) bonds (ν_s(O-W-O)) [8, 14, 27, 31, 32, 34-36, 41-43]; the peaks at 276 and 330 cm^{-1} are associated with bending vibration of (O-W-O) bonds (δ(O-W-O)) [3, 8, 14, 27, 31, 32, 34, 42, 43]; and the lower frequency peak (190 cm^{-1}) can be assigned to lattice modes of monoclinic WO_3 [34]. The small shoulder located at ~640 cm^{-1} cannot be assigned to monoclinic WO_3 and has been attributed to the O-W-O symmetric stretching vibration of the bridging oxygen in the residual hydrated WO_3 [32], similar to the band observed for $WO_3 \cdot 2H_2O$ (**Figure 1a**). Hence, after subjecting the samples to a heat treatment at 400º C for 4 hours, the hydrated species, mainly $WO_3 \cdot 2H_2O$, will convert into crystalline monoclinic WO_3 through dehydration of hydroxyl groups [27, 28].

3.2. Morphological characterization of the formed nanostructures.

Figure 2 shows the FE-SEM images of the samples anodized in 1.5M H_2SO_4 solution at 0 and 2000 rpm, in the absence and presence of fluoride anions, and **Table 1** gathers the main dimensions of the nanostructures obtained under different conditions. In all cases, the nanostructures formed on the W surface present nanoplatelet morphology, as other authors reported when anodizing in similar acid electrolytes [3, 9, 12, 13, 19]. In the electrolyte without 0.1M NaF and 0 rpm (**Figure 2a**), nanoplatelets grew quite orderly and almost orthogonal to the electrode surface.

In the same electrolyte (without F^-) but under hydrodynamic conditions (2000 rpm, **Figure 2b**) it can be observed that nanoplatelets lost their perpendicularity and ordered distribution, growing in a quite random way; besides, the dimensions of these nanoplatelets also changed as a consequence of rotation (**Table 1**), with their length slightly decreasing and the thickness of the nanoplatelet layer increasing significantly. Hydrodynamic conditions can influence the growth of nanoplalets in two opposite ways: on the one hand, mechanical convection (stirring) reduces the concentration of soluble species close to the electrode surface, hence decreasing the nanoplatelets growth rate by precipitation [9, 26]; on the other hand, hydrodynamic conditions enhance mass transfer towards the electrode surface, thus favoring the formation of soluble species responsible for the formation of nanoplatelets. In this case, according to the data shown in **Table 1**, it is the second factor (the enhancement of mass transfer) that had more

influence on the formation and growth of nanoplatelets, since the thickness of the WO_3 layer is higher at 2000 rpm.

In the presence of 0.1M NaF under stagnant conditions (**Figure 2c**), the surface was also covered with ordered nanoplatelets, although multiple cracks going crisscrossed the whole surface (**Figure 2d**). On the other hand, it can be observed that all the dimensions of nanoplatelets were larger than those obtained without F^- at 0 rpm (**Table 1**). This fact can be explained taking into account that, apart from the acid dissolution of WO_3 to give WO_2^{2+} (reaction (2)), in the presence of F^- these anions also attacked the tungsten surface, leading to the localized dissolution of WO_3 into soluble fluoride complexes, according to [4, 28, 40]:

$$WO_3 + 6H^+ + nF^- \rightarrow [WF_n]^{(n-6)} + 3H_2O \quad \textbf{(5)}$$

The combination of reactions (2) and (5) resulted in an increase of the concentration of soluble species released from the electrode surface, contributing to the enhancement of the nucleation and growth rate of nanoplatelets (by precipitation, reaction (3)). This, in turn, led to an increase in nanoplatelets size [9, 26], since formation of nanoplatelets involves the nucleation of primary particles induced by supersaturation conditions followed by their aggregation [9]. Therefore, the higher the amount of soluble species accumulating near the electrode surface, the larger the dimensions of the nanoplatelets formed by precipitation of these soluble species.

In the same electrolyte solution (with F^-) but under hydrodynamic conditions (2000 rpm, **Figure 2e**), the distribution of nanoplatelets clearly changed: in this case,

nanoplatelets grew in a very peculiar manner, forming clusters between them resembling trees, which made this new nanoplatelet configuration expose much more active area to the electrolyte than normal nanoplatelets described above. Nanoplatelets dimensions also changed in this case (**Table 1**): their length slightly decreased with respect to the test in the same F^- electrolyte but at 0 rpm, and the overall layer thickness increased significantly. This increase in the nanoplatelet layer thickness is directly related to an increase in the growth rate, as explained above. Although stirring could reduce the concentration of soluble species near the electrode surface, in this case the presence of F^-, together with the enhancement of mass transfer towards the surface, resulted in higher amounts of soluble species released from the substrate. Nevertheless, due to the characteristics of the flow velocity in the radial direction close to the surface of an RDE, this type of nanostructure was only formed in an approximately circular region located at the center of the electrode (the covered area was ~2 mm in diameter, which represents only the 6.3% of the total surface).

In an RDE, its rotational motion drives the electrolyte from the bulk towards the electrode along the *y*-axis perpendicular to the surface and, due to centrifugal force, flings the electrolyte outward from the center radially across the electrode surface. Near the surface of the rotating electrode, the flow velocities in the direction normal to the surface, υ_y, and in the radial direction, υ_r, are given by [44]:

$$\upsilon_y = -0.51\omega^{3/2}\nu^{-1/2}y^2 \quad \textbf{(6)}$$

$$\upsilon_r = 0.51\omega^{3/2}\nu^{-1/2}ry \quad \textbf{(7)}$$

where ω is the angular velocity, ν the kinematic viscosity of the fluid, and y and r are, in cylindrical coordinates, the distance from the electrode surface in the normal direction and the distance from the rotation axis in the radial direction, respectively. It can be observed that both υ_y and υ_r increase (in absolute value) with increasing the rotation velocity (ω). Besides, for given values of y and ω in a certain electrolyte, υ_y is constant but υ_r still depends on r and increases with increasing distance from the electrode rotation axis. Hence, the centrifugal forces of the rotation lead to a constant increase of the electrolyte velocity towards the outer edge of electrode surface.

As explained above, for nanoplatelets to form on the electrode surface, supersaturation conditions of the soluble species near the electrode must be reached. These supersaturation conditions, with the electrode rotating at 2000 rpm, were only achieved in a more or less circular area around the rotation axis (low values of r in eq. (7)), where the fluid velocity in the radial direction was low enough to prevent soluble species from being completely swept away from the vicinity of the electrode surface.

Figure 3 shows FESEM images of the peripheral region of the surface of the sample anodized in the presence of F^- at 2000 rpm (**Figures 3a** and **3b**), which is clearly different from that observed in the central region **(Figure 3c**). In the peripheral region, craters or pores of different dimensions can be observed on the electrode surface (**Figure 3a**), most of them being more than 1 μm in diameter. This morphology is a consequence of localized WO_3 dissolution by the action of fluoride anions (see eq. (5)), without the subsequent precipitation of soluble species to form $WO_3 \cdot 2H_2O$ due to the impossibility of reaching supersaturation conditions at distances from the rotation axis of r > ~1 mm. Hence, nanoplatelets were not formed in the outer region of the surface,

although some small but well defined nanoplatelets can still be observed at the bottom of the deepest craters or pores (**Figure 3b**). The formation of these nanostructures inside deep craters can also be explained in terms of the supersaturation conditions necessary for soluble species to precipitate. These conditions, far from the rotation axis, could only be established at the bottom of these craters, where high concentrations of soluble species released from the surface were locally maintained without the influence of flux velocity.

With the aim of decreasing the velocity of the electrolyte in the radial direction, and hence of increasing the extent of the electrode surface covered by the new nanostructure, without altering its morphology (i.e. tree-like nanoplatelets clusters), anodization of W was also carried out reducing the rotation velocity to 500 rpm, in the same solution (1.5M H_2SO_4 with 0.1M NaF at 50º C) and keeping the same conditions of applied potential and anodization time. **Figure 4** shows FESEM images of the electrode surface after anodization under the new hydrodynamic conditions (500 rpm). In this case, the dimensions of the circular area covered with nanoplatelets was quantified to be ~6.5 mm in diameter, the 66% of the total surface, which is significantly higher than the 6.3% of covered surface obtained at 2000 rpm. Therefore, by decreasing the electrode rotation velocity, the fluid velocity in the radial direction was also reduced (eq. (7)), which favored the creation of supersaturation conditions of soluble species at longer distances *r* from the rotation axis.

In the outermost region of the electrode surface, craters or pores of different size can be observed (**Figure 4a**), but their number is notably lower than at 2000 rpm, as well as their depth (see **Figure 3a** to compare). This fact is also a consequence of reducing the

rotation speed, since at 2000 rpm the diffusion layer thickness was reduced with respect to 500 rpm. Hence, at 2000 rpm, F^- ions were permitted to diffuse to the electrode surface more rapidly, thus enhancing the dissolution of the WO_3 layer via reaction (5) and increasing the number and size of craters or pores resulting from that dissolution. In the outer region of the surface, the formation of small nanoplatelets can also be observed at the bottom of craters or pores (**Figure 4b**).

Concerning the morphology of the nanostructures formed on the covered region of the surface, it is similar to that observed at 2000 rpm (see **Figure 2e**), where nanoplatelets grew in a tree-like fashion, forming compact clusters that resemble a coniferous forest seen from above or some coral reef (**Figure 4c** and **Figure 4d**). Nevertheless, at 500 rpm, this new nanostructure is more compact and the size of nanoplatelets clusters is larger than at 2000 rpm (compare **Figure 4c** (at 500 rpm) with **Figure 3c** (at 2000 rpm)). Besides, the nanoplatelets layer is also thicker in this case (**Table 1**), so the active area in contact with the electrolyte is even higher than at 2000 rpm. The thickness of this layer can be observed in the cross sectional view shown in **Figure 4e**.

The question that now arises is why the influence of fluid velocity in the radial direction on the dissolution/precipitation process leading to the formation of $WO_3 \cdot 2H_2O$ nanoplatelets does not appear in the F^--free electrolytes where the whole electrode surface was covered with nanoplatelets at 2000 rpm. To answer this question, the joint action of F^- and flowing conditions must be taken into account. Due to the rotation of the electrode, formation of nanoplatelets on the outer part of the electrodes was more difficult under hydrodynamic conditions, as explained above; on the other hand, the smaller number of nanoplatelets formed at a certain distance *r* from the rotation axis

underwent dissolution by the action of F^- (reaction (5)). Hence, anodization without the influence of F^- did not result in different nanoplatelet distribution or different extent of covered surface depending on the hydrodynamic conditions, i.e., the extent of surface covered by nanoplatelets in the absence of fluoride anions was 100% at 0 and 2000 rpm.

3.3. Analysis of the current density transients during anodization.

The current density transient recorded during anodization provides useful information on the electrochemical processes taking place on the electrode surface. Current density transients for all the samples are presented in **Figure 5**. In all cases, current density sharply decreased during the first seconds of anodization, indicating the formation of a WO_3 layer on the surface [16, 23, 40].

In the electrolytes without F^- ions, current density started increasing again after approximately 18 minutes (at 0 rpm) and 13 minutes (at 2000 rpm), due to the dissolution of the WO_3 layer (reaction (2)). Besides, current densities recorded at 2000 rpm were higher than at 0 rpm, indicating that the dissolution of the substrate via reaction (2) was faster under hydrodynamic conditions. This fact can be related to an enhancement in the mass transfer with increasing rotation velocity. Subsequently, current density started decreasing after reaching a maximum peak (at 0 rpm) or after remaining more or less constant for more than 1 hour and 30 minutes (2000 rpm). This region of maximum current density and the following decrease is directly associated with the formation and growth of hydrated WO_3 in form of nanoplatelets on the electrode surface, according to reactions (3) and (4). As the precipitated layer became thicker and blocked the electrochemical active area, the rate of substrate oxidation

(reaction (1)) and dissolution (reaction (2)) decreased, and hence current density also decreased. Finally, current density reached a constant value until the end of the anodization process, indicating that a steady-state between substrate oxidation/dissolution and $WO_3 \cdot 2H_2O$ nanoplatelets formation by precipitation was established.

In the presence of 0.1M NaF and at 0 rpm, after the initial drop due to the formation of a WO_3 layer, current density rapidly increased, reached a maximum peak and decreased again. Finally, it reached a constant and relatively low value until the end of the process. The overall shape of this curve is quite similar as that observed before for the electrolytes without fluorides, so the explanations are the same: while the W substrate underwent oxidation to form WO_3, WO_2^{2+} and other soluble species were continuously released from the electrode by the reaction of H^+ and F^- with the oxide (reactions (2) and (5), respectively); afterward these soluble species precipitated on the electrode surface, upon reaching supersaturation conditions, in form of hydrated WO_3 nanoplatelets. Eventually, a steady-state between dissolution/precipitation was attained. It is worth mentioning that in the presence of F^- ions, current densities during the dissolution process were higher than in the absence of F^- ions, which is consistent with an enhancement of soluble species formation and with the larger size of nanoplatelets formed in the electrolyte with 0.1M NaF (**Table 1**).

In the F^--containing electrolytes under hydrodynamic conditions (500 and 2000 rpm), the initial decrease in current density and the subsequent peak indicating the formation of nanoplatelets can also be discerned. However, after the peak in current density, the features of the transients are considerably different from those commented above. In

both cases, current densities were very high during the 4 hours of anodization, and the signals were markedly noisy. These fluctuations in the current density signal are similar to those widely observed for stainless steels and other metals and alloys in the presence of halides and other aggressive anions, ascribed to the occurrence of metastable pits on the electrode surface [45-51], which are small pits that nucleate and rapidly repassivate [52]. In this case, these fluctuations are associated with a competition between the local dissolution of the oxide via reactions (2) and (5) (especially due to the action of F^-), which exposes bare W surface to the electrolyte, and the continuous formation of WO_3 via substrate oxidation at these local sites (reaction (1)) and via precipitation of soluble species (reactions (3) and (4)). In the electrolyte without F^-, at 2000 rpm, smaller fluctuations can also be observed, indicating that the acidic dissolution of the substrate (reaction (2)) also took place locally and that this dissolution was enhanced under hydrodynamic conditions.

3.4. Photoelectrochemical measurements.

Figure 6 shows the photocurrent density transients of the different annealed WO_3 nanostructures as a function of the applied potential. It can be observed that for the samples anodized without NaF, hydrodynamic conditions positively affected their photoelectrochemical performance, since photocurrents recorded upon illumination were visibly higher at 2000 rpm than at 0 rpm. This can be ascribed to the higher thickness of the nanoplatelets layer formed at 2000 rpm without F^- (**Table 1**). Therefore, in spite of nanoplatelets growing more ordered and perpendicular to the surface at 0 rpm, it seems that the increase in WO_3 layer thickness observed at 2000 rpm may

enhance the exposed surface area of this sample, resulting in higher photoelectrochemical activity.

On the other hand, for samples anodized in the presence of F^-, it can be seen that at 0 rpm, photocurrent densities were similar as those obtained in the absence of F^- under the same static conditions. Hence, although nanoplatelets formed in the F^--containing electrolyte were larger and the thickness of the WO_3 nanoplatelets layer was higher than in the F^--free electrolyte (**Table 1**), it is evident that the irregularity of the surface at 0 rpm with F^-, where deep cracks could be discerned throughout the electrode surface (**Figure 2d**), negatively contributed to the photoelectrochemical response of the sample. As a consequence, in spite of the higher surface area of nanoplatelets formed in the solution with F^-, photocurrent densities did not follow the same pattern.

In the presence of F^- at 2000 rpm, the photoresponse of the electrode was very low, compared with the rest of samples. This fact is directly related to the small surface area covered by nanoplatelets, which was quantified to be ~ 0.03 cm^2, while the total area exposed to the electrolyte in the photoelectrochemical tests was 0.13 cm^2. This means that a portion of the uncovered area with craters or pores (see **Figure 3a**) was also in contact with the electrolyte and irradiated, so the photoresponse of this sample had two contributions: one of the active area covered by nanoplatelets (~ 0.03 cm^2) and another of the quite inactive area (compact WO_3 layer) uncovered by nanoplatelets and with craters or pores (~ 0.1 cm^2).

In contrast, photocurrent densities for the sample anodized in the presence of F^- at 500 rpm were very large. In this case, the area covered by nanoplatelets was ~ 0.33 cm^2,

higher than the area exposed to the electrolyte (0.13 cm^2). Hence, the photoresponse of this sample corresponded only to the surface covered by nanoplatelet clusters associated in a tree-like fashion. With this morphology, as explained above, the active area in contact with the electrolyte was extraordinarily large, which is reflected in the very high photocurrent densities.

Conclusions

As-anodized samples consisted of hydrated WO_3, mainly $WO_3 \cdot 2H_2O$. After annealing the samples, monoclinic WO_3 phase was obtained.

WO_3 nanoplatelets were obtained in all the cases, regardless of the electrolyte and the rotation velocity used during anodization. Nevertheless, the morphology, dimensions and distribution of these nanoplatets strongly depended on the electrolyte composition and hydrodynamic conditions, since the formation and growth of WO_3 nanoplatelets followed a dissolution/precipitation mechanism.

Hydrodynamic conditions enhanced mass transfer towards the electrode, thus favoring the dissolution of the W substrate. In the presence of F^- and under electrode rotation, this dissolution was greatly enhanced, and novel tree-like nanoplatelets clusters with very large surface area were obtained.

The active area of the new nanostructure growing in a tree-like fashion in contact with the electrolyte was extraordinarily large, so photocurrent densities obtained for this

morphology were very high compared with the rest of the samples. Future work must be carried out to optimize the synthesis of the new nanostructure.

Acknowledgements: Authors would like to express their gratitude for the financial support to the Ministerio of Economía y Competitividad (Project CTQ2013-42494-R) and for its help in the Laser Raman Microscope acquisition (UPOV08-3E-012).

REFERENCES

[1] H. Zheng, J. Z. Ou, M. S. Strano, R. B. Kaner, A. Mitchell, K. Kalantar-zadeh. Nanostructured Tungsten Oxide - Properties, Synthesis, and Applications, Adv. Funct. Mater. 21 (2011) 2175-2196.

[2] K. Kalantar-zadeh, A. Vijayaraghavan, M.H. Ham, H. Zheng, M. Breedon, M. S. Strano. Synthesis of Atomically Thin WO_3 Sheets from Hydrated Tungsten Trioxide, Chem. Mater. 22 (2010) 5660-5666.

[3] A. Z. Sadek, H. Zheng, M. Breedon, V. Bansal, S. K. Bhargava, K. Latham, J. Zhu, L. Yu, Z. Hu, P. G. Spizzirri, W. Wlodarski, K. Kalantar-zadeh. High-Temperature Anodized WO_3 Nanoplatelet Films for Photosensitive Devices, Langmuir 25 (2009) 9545-9551.

[4] C. W. Lai, S. Sreekantan. Fabrication of WO_3 nanostructures by anodization method for visible-light driven water splitting and photodegradation of methyl orange, Mat. Sci. Semicon. Proc. 16 (2013) 303-310.

[5] H. Zheng, Y. Tachibana, K. Kalantar-zadeh. Dye-Sensitized Solar Cells Based on WO_3, Langmuir 26 (2010) 19148-19152.

[6] V. Cristino, S. Caramori, R. Argazzi, L. Meda, G. L. Marra, C. A. Bignozzi. Efficient Photoelectrochemical Water Splitting by Anodically Grown WO_3 Electrodes, Langmuir 27 (2011) 7276-7284.

[7] C. W. Lai. Photocatalysis and Photoelectrochemical Properties of Tungsten Trioxide Nanostructured Films, The Scientific World J. 2014 (2014) 843587 (7pp).

[8] H. Song, Y. Li, Z. Lou, M. Xiao, L. Hu, Z. Ye, L. Zhu. Synthesis of Fe-doped WO_3 nanostructures with high visible-light-driven photocatalytic activities, Appl. Catal. B-Environ. 166-167 (2015) 112-120.

[9] C. Ng, C. Ye, Y. H. Ng, R. Amal. Flower-Shaped Tungsten Oxide with Inorganic Fullerene-like Structure: Synthesis and Characterization, Cryst. Growth Des. 10 (2010) 3794-3801.

[10] Y. C. Nah, A. Ghicov, D. Kim, P. Schmuki. Enhanced electrochromic properties of self-organized nanoporous WO_3, Electrochem. Commun. 10 (2008) 1777-1780.

[11] J. Z. Ou, S. Balendhran, M. R. Field, D. G. McCulloch, A. S. Zoolfakar, R. A. Rani, S. Zhuiykov, A. P. O'Mullane, K. Kalantar-zadeh. The anodized crystalline WO_3 nanoporous network with enhanced electrochromic properties, Nanoscale 4 (2012) 5980-5988.

[12] J. Z. Ou, M. Z. Ahmad, K. Latham, K. Kalantar-zadeh, G. Sberveglieri, W. Wlodarski. Synthesis of the nanostructured WO_3 via anodization at elevated temperature for H_2 sensing applications, Procedia Engineering 25 (2011) 247-251.

[13] K. Kalantar-zadeh, A. Z. Sadek, H. Zheng, V. Bansal, S. K. Bhargava, W. Wlodarski, J. Zhu, L. Yu, Z. Hu. Nanostructured WO_3 films using high temperature anodization, Sensor. Actuat. B-Chem. 142 (2009) 230-235.

[14] J. Z. Ou, M. H. Yaacob, J. L. Campbell, M. Breedon, K. Kalantar-zadeh, W. Wlodarski. H_2 sensing performance of optical fiber coated with nano-platelet WO_3 film, Sensor. Actuat. B-Chem. 166-167 (2012) 1-6.

[15] N. R. de Tacconi, C. R. Chenthamarakshan, G. Yogeeswaran, A. Watcharenwong, R. S. de Zoysa, N. A. Basit, K. Rajeshwar. Nanoporous TiO_2 and WO_3 Films by Anodization of Titanium and Tungsten Substrates: Influence of Process Variables on Morphology and Photoelectrochemical Response, J. Phys. Chem. B 110 (2006) 25347-25355.

[16] W. Wei, S. Shaw, K. Lee, P. Schmuki. Rapid Anodic Formation of High Aspect Ratio WO_3 Layers with Self-Ordered Nanochannel Geometry and Use in Photocatalysis, Chem. Eur. J. 18 (2012) 14622-14626.

[17] S. S. Kalanur, Y. J. Hwang, S. Y. Chae, O. S. Joo. Facile growth of aligned WO_3 nanorods on FTO substrate for enhanced photoanodic water oxidation activity, J. Mater. Chem. A 1 (2013) 3479-3488.

[18] Q. Chen, J. Li, B. Zhou, M. Long, H. Chen, Y. Liu, W. Cai, W. Shangguan. Preparation of well-aligned WO_3 nanoflake arrays vertically grown on tungsten substrate as photoanode for photoelectrochemical water splitting, Electrochem. Commun. 20 (2012) 153-156.

[19] C. Ng, Y. H. Ng, A. Iwase, R. Amal. Influence of Annealing Temperature of WO_3 in Photoelectrochemical Conversion and Energy Storage for Water Splitting, ACS Appl. Mater. Inter. 5 (2013) 5269-5275.

[20] J. Z. Ou, R. A. Rani, S. Balendhran, A. S. Zoolfakar, M. R. Field, S. Zhuiykov, A. P. O'Mullane, K. Kalantar-zadeh. Anodic formation of a thick three-dimensional nanoporous WO_3 film and its photocatalytic property, Electrochem. Commun. 27 (2013) 128-132.

[21] A. Tacca, L. Meda, G. L. Marra, A. Savoini, S. Caramori, V. Cristino, C. A. Bignozzi, V. G. Pedro, P. P. Boix, S. Gimenez, J. Bisquert. Photoanodes Based on Nanostructured WO_3 for Water Splitting, ChemPhysChem 13 (2012) 3025-3034.

[22] K. R. Reyes-Gil, C. Wiggenhorn, B. S. Brunschwig, N. S. Lewis. Comparison between the Quantum Yields of Compact and Porous WO_3 Photoanodes, J. Phys. Chem. C 117 (2013) 14947-14957.

[23] H. Tsuchiya, J. M. Macak, I. Sieber, L. Taveira, A. Ghicov, K. Sirotna, P. Schmuki. Self-organized porous WO_3 formed in NaF electrolytes, Electrochem. Commun. 7 (2005) 295-298.

[24] Y. Liu, Y. Li, W. i, S. an, C. iu. Photoelectrochemical properties and photocatalytic activity of nitrogen-doped nanoporous WO_3 photoelectrodes under visible light, Appl. Surf. Sci. 258 (2012) 5038-5045.

[25] Y. C. Nah, I. Paramasivam, R. Hahn, N. K. Shrestha, P. Schmuki. Nitrogen doping of nanoporous WO_3 layers by NH_3 treatment for increased visible light photoresponse, Nanotechnology 21 (2010) 105704 (5pp).

[26] E. Widenkvist, R. A. Quinlan, B. C. Holloway, H. Grennberg, U. Jansson. Synthesis of Nanostructured Tungsten Oxide Thin Films, Cryst. Growth Des. 8 (2008) 3750-3753.

[27] F. Amano, M. Tian, B. Ohtani, A. Chen. Photoelectrochemical properties of tungsten trioxide thin film electrodes prepared from facet-controlled rectangular platelets, J. Solid State Electrochem. 16 (2012) 1965-1973.

[28] C. K. Wang, C. K. Lin, C. L. Wu, S. C. Wang, J. L. Huang. Synthesis and characterization of electrochromic plate-like tungsten oxide films by acidic treatment of electrochemical anodized tungsten, Electrochim. Acta 112 (2013) 24-31.

[29] A. Di Paola, F. Di Quarto, C. Sunseri. Anodic oxide films on tungsten—I. The influence of anodizing parameters on charging curves and film composition, Corros. Sci. 20 (1980) 1067-1078.

[30] R. Sánchez-Tovar, R. M. Fernández-Domene, D. M. García-García, J. García-Antón. Enhancement of photoelectrochemical activity for water splitting by controlling hydrodynamic conditions on titanium anodization, J. Power Sources 286 (2015) 224-231.

[31] C. Bittencourt, R. Landers, E. Llobet, X. Correig, J. Calderer. The role of oxygen partial pressure and annealing temperature on the formation of W = O bonds in thin WO_3 films, Semicond. Sci. Technol. 17 (2002) 522-525.

[32] C. Santato, M. Odziemkowski, M. Ulmann, J. Augustynski. Crystallographically Oriented Mesoporous WO_3 Films: Synthesis, Characterization, and Applications, J. Am. Chem. Soc. 123 (2001) 10639-10649.

[33] B. Pecquenard, H. Lecacheux, J. Livage, C. Julien. Orthorhombic WO_3 Formed via a Ti-Stabilized $WO_3 \cdot 13H_2O$ Phase, J. Solid State Chem. 135 (1998) 159-168.

[34] M. F. Daniel, B. Desbat, J. C. Lassegues, B. Gerand, M. Figlarz. Infrared and Raman study of WO_3 tungsten trioxides and WO_3, xH_2O tungsten trioxide tydrates, J. Solid State Chem. 67 (1987) 235-247.

[35] J. Díaz-Reyes, V. Dorantes-García, A. Pérez-Benítez, J. A. Balderas-López. Obtaining of films of tungsten trioxide (WO_3) by resistive heating of a tungsten filament, Superficies y Vacío 21 (2008) 12-17.

[36] S. H. Lee, H. M. Cheong, C. E. Tracy, A. Mascarenhas, D. K. Benson, S. K. Deb. Raman spectroscopic studies of electrochromic a-WO_3, Electrochim. Acta 44 (1999) 3111-3115.

[37] S. H. Lee, H. M. Cheong, C. E. Tracy, A. Mascarenhas, A. W. Czanderna. Electrochromic coloration efficiency of a-WO_{3-y} thin films as a function of oxygen deficiency, Appl. Phys. Lett. 75 (1999) 1541-1543.

[38] M. Boulova, G. Lucazeau. Crystallite Nanosize Effect on the Structural Transitions of WO_3 Studied by Raman Spectroscopy, J. Solid State Chem. 167 (2002) 425-434.

[39] A. G. Souza-Filho, V. N. Freire, J. M. Sasaki, J. Mendes Filho, J. F. Julião, U. U. Gomes. Coexistence of triclinic and monoclinic phases in WO_3 ceramics, J. Raman Spectrosc. 31 (2000) 451-454.

[40] W. Li, J. Li, X. Wang, S. Luo, J. Xiao, Q. Chen. Visible light photoelectrochemical responsiveness of self-organized nanoporous WO3 films, Electrochim. Acta 56 (2010) 620-625.

[41] Z. Lu, S. M. Kanan, C. P. Tripp. Synthesis of high surface area monoclinic WO_3 particles using organic ligands and emulsion based methods, J. Mater. Chem. 12 (2002) 983-989.

[42] L. Xu, M. L. Yin, S. Liu. $Ag_x@WO_3$ core-shell nanostructure for LSP enhanced chemical sensors, Sci. Rep. 4 (2014) 6745 (7pp).

[43] A. Rougier, F. Portemer, A. Quédé, M. El Marssi. Characterization of pulsed laser deposited WO_3 thin films for electrochromic devices, Appl. Surf. Sci. 153 (1999) 1-9.

[44] A. J. Bard and L. R. Faulkner, Electrochemical Methods: Fundamentals and Applications, John Wiley & Sons, New York, NY, 2001.

[45] M. H. Moayed, N. J. Laycock, R. C. Newman. Dependence of the Critical Pitting Temperature on surface roughness, Corros. Sci. 45 (2003) 1203-1216.

[46] J. B. Lee, S. I. Yoon. Effect of nitrogen alloying on the semiconducting properties of passive films and metastable pitting susceptibility of 316L and 316LN stainless steels, Mater. Chem. Phys. 122 (2010) 194-199.

[47] M. A. Amin. Metastable and stable pitting events on Al induced by chlorate and perchlorate anions--Polarization, XPS and SEM studies, Electrochim. Acta 54 (2009) 1857-1863.

[48] L. F. Garfias-Mesias, J. M. Sykes. Metastable pitting in 25 Cr duplex stainless steel, Corros. Sci. 41 (1999) 959-987.

[49] P. Ernst, R. C. Newman. Pit growth studies in stainless steel foils. I. Introduction and pit growth kinetics, Corros. Sci. 44 (2002) 927-941.

[50] R. M. Fernández-Domene, E. Blasco-Tamarit, D. M. García-García, J. García-Antón. Repassivation of the damage generated by cavitation on UNS N08031 in a LiBr solution by means of electrochemical techniques and Confocal Laser Scanning Microscopy, Corros. Sci. 52 (2010) 3453-3464.

[51] R. M. Fernández-Domene, E. Blasco-Tamarit, D. M. García-García, J. García-Antón. Cavitation corrosion and repassivation kinetics of titanium in a heavy brine LiBr solution evaluated by using electrochemical techniques and Confocal Laser Scanning Microscopy, Electrochim. Acta 58 (2011) 264-275.

[52] H. Böhni, Localized Corrosion of Passive Metals, in: R. Winston Revie (Ed.), Uhlig's Corrosion Handbook, 2nd edition, in: R.Winston Revie (ed.), Uhlig's Corrosion Handbook, New York, 2000, 173-190.

Table caption

Table 1. Main dimensions of the nanostructures obtained under different conditions.

Figures captions

Figure 1. Raman spectra of the (a) as-anodized samples, and (b) after the heat treatment at 400º C for 4 h.

Figure 2. FESEM images of nanostructures formed upon anodization of W in a 1.5M H_2SO_4 electrolyte at 50º C, imposing a potential of 20V for 4 hours, under different hydrodynamic conditions and fluoride concentration: (a) and (c) 0 rpm without and with 0.1M NaF, respectively; (b) and (e) 2000 rpm without and with 0.1M NaF, respectively; (d) general view of the sample anodized at 0 rpm with 0.1M NaF.

Figure 3. FESEM images of the sample surface after anodization in a 1.5M H_2SO_4 with 0.1M NaF electrolyte at 50º C, imposing a potential of 20V for 4 hours, and under a rotation speed of 2000 rpm. (a) Image of the outer part of the electrode surface showing many craters or pores of different size; (b) detail of a deep crater (or pore) in whose bottom nanoplatelets could form; (c) image of the covered part of the electrode (which represents the 6.3% of the total surface area).

Figure 4. FESEM images of the sample surface after anodization in a 1.5M H_2SO_4 with 0.1M NaF electrolyte at 50º C, imposing a potential of 20V for 4 hours, and under a rotation speed of 500 rpm. (a) Image of the outer part of the electrode surface showing some craters or pores of different size; (b) detail of the outer part surface, where the formation of small nanoplatelets can be observed; (c) image of the covered part of the electrode (which represents the 66% of the total surface area); (d) detail of the formed nanostructure in the covered part; (e) cross sectional view of the WO_3 nanoplatelets layer.

Figure 5. Current density transient recorded during anodization for all the samples.

Figure 6. Photocurrent density transients of the different annealed WO_3 nanostructures measured in a 0.1M H_2SO_4 solution under AM1.5 illumination, as a function of the applied potential.

Table 1

Anodization conditions	Platelet thickness/nm	Platelet length/nm	WO_3 layer thickness/nm
0 rpm without NaF	32 ± 6	389 ± 74	435 ± 35
2000 rpm without NaF	30 ± 3	339 ± 64	1943 ± 166
0 rpm with 0.1M NaF	36 ± 3	615 ± 71	1929 ± 114
2000 rpm with 0.1M NaF	40 ± 4	523 ± 58	3481 ± 170
500 rpm with 0.1M NaF	42 ± 6	555 ± 88	7644 ± 374

Figure 1

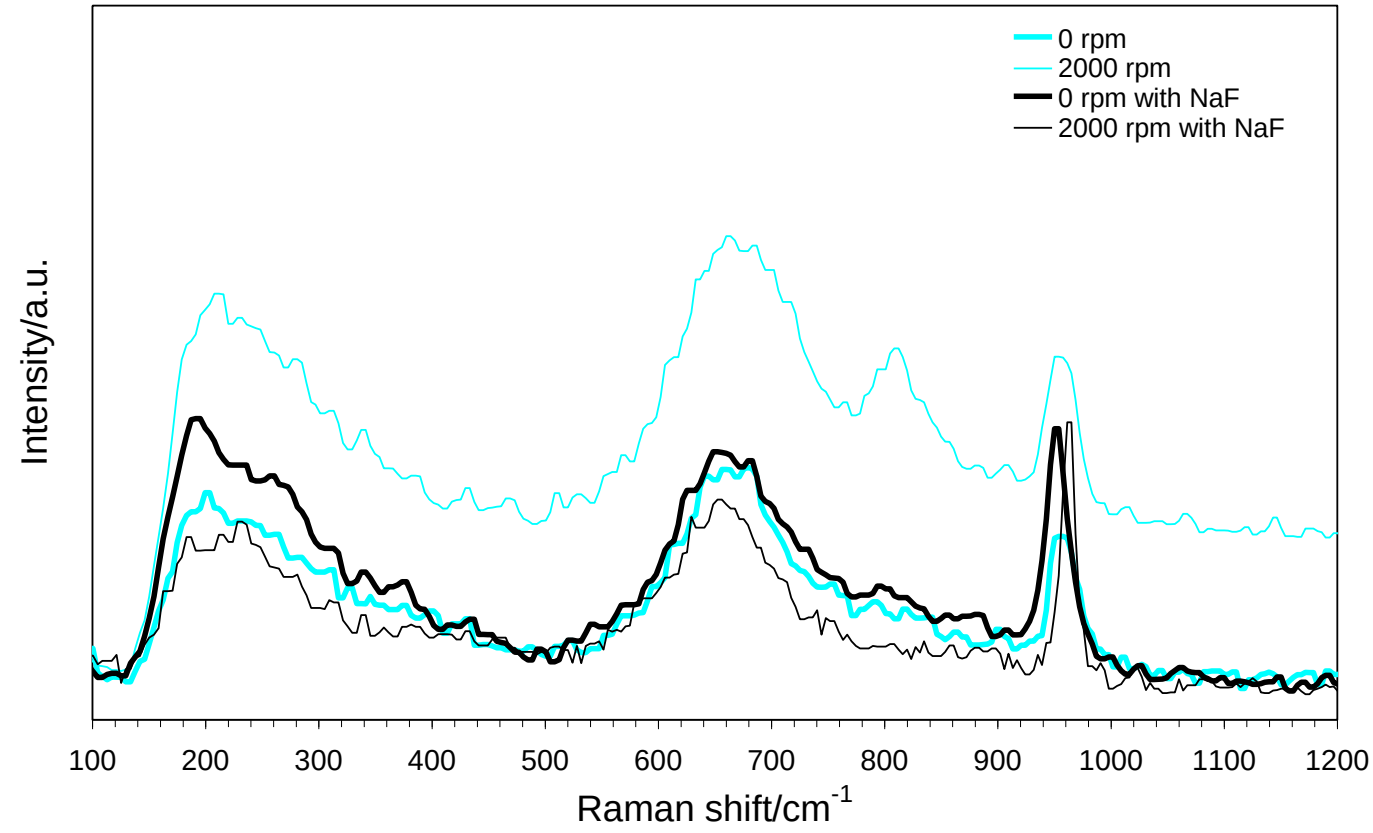
0 rpm
2000 rpm
0 rpm with NaF
2000 rpm with NaF
Intensity/a.u.
100
200
300
400
500
600
700
800
900
1000
1100
1200
Raman shift/cm-1

(a)

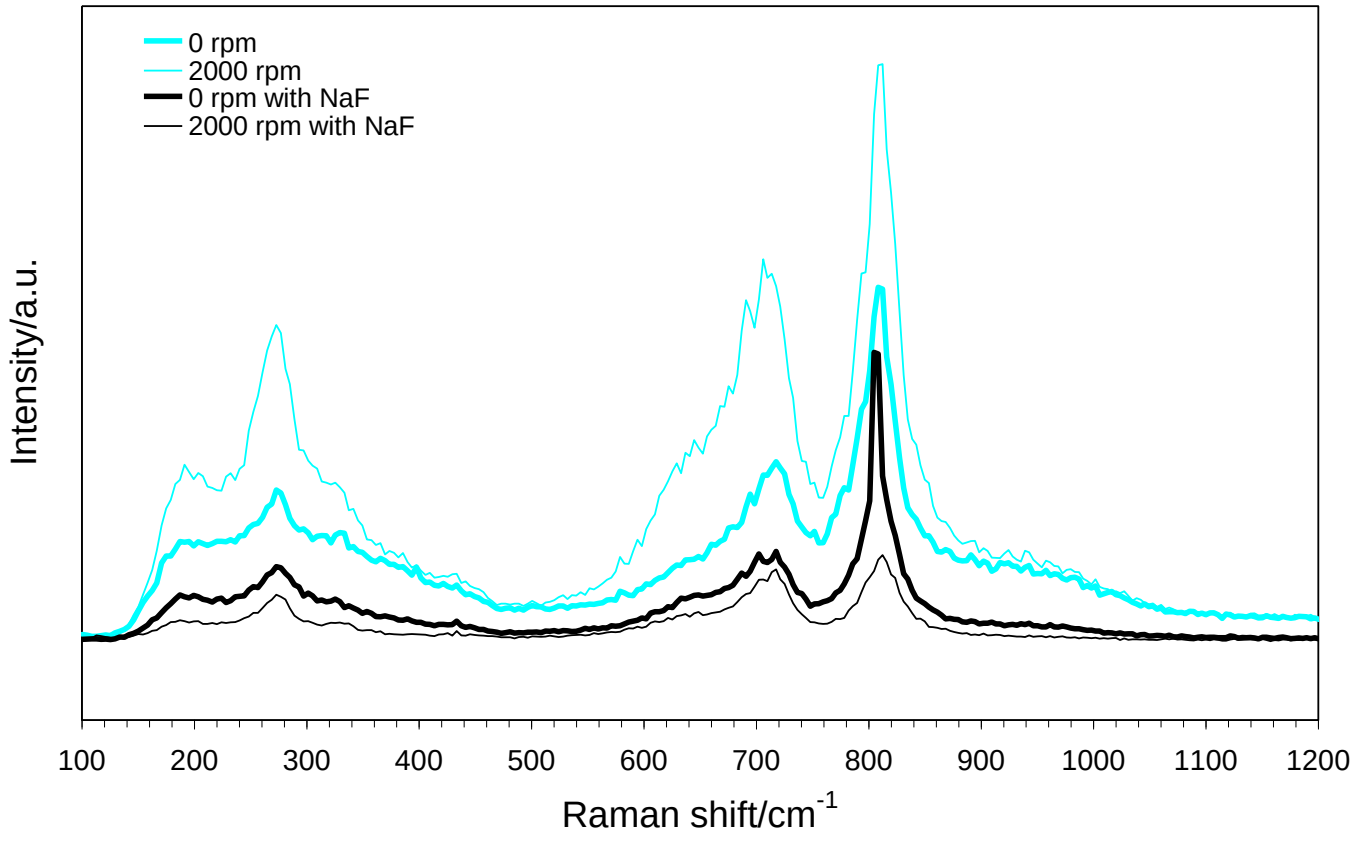
0 rpm
2000 rpm
0 rpm with NaF
2000 rpm with NaF
Intensity/a.u.
100
200
300
400
500
600
700
800
900
1000
1100
1200
Raman shift/cm-1

(b)

Figure 2

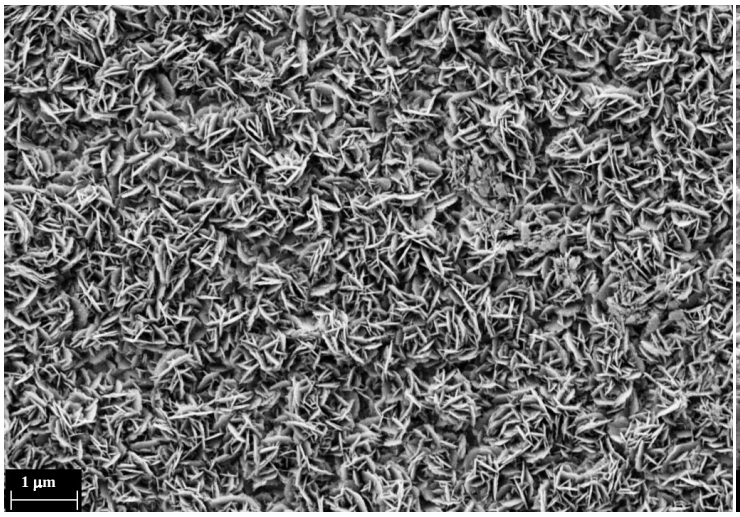

(a)

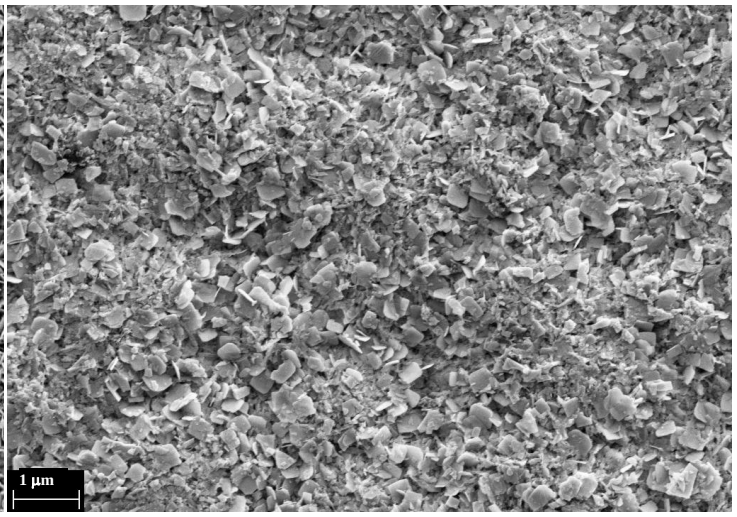

(b)

(c)

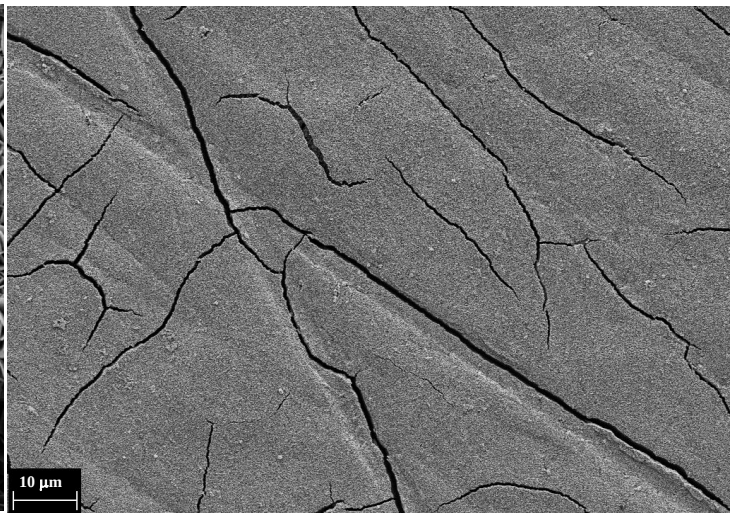

(d)

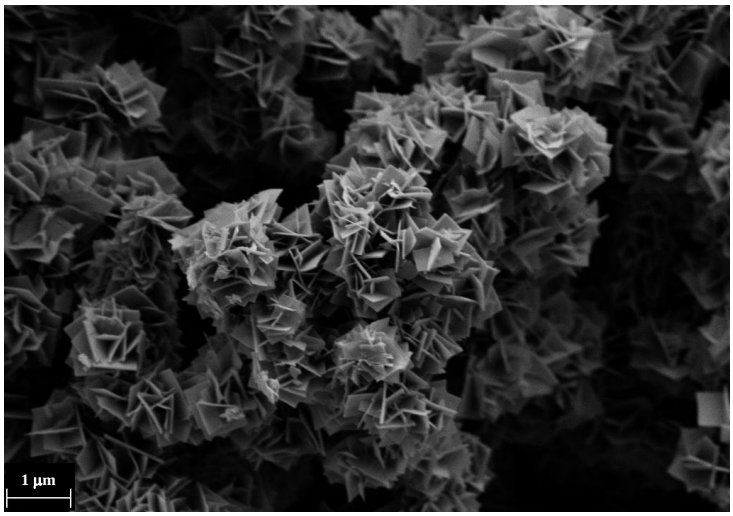

(e)

Figure 3

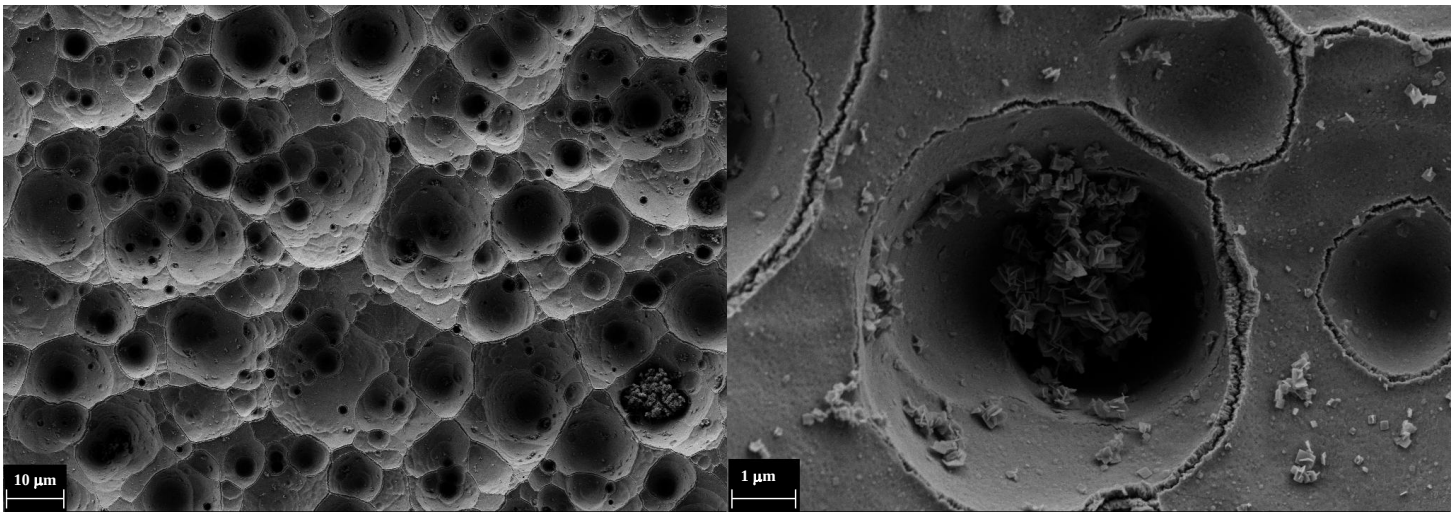

(a) **(b)**

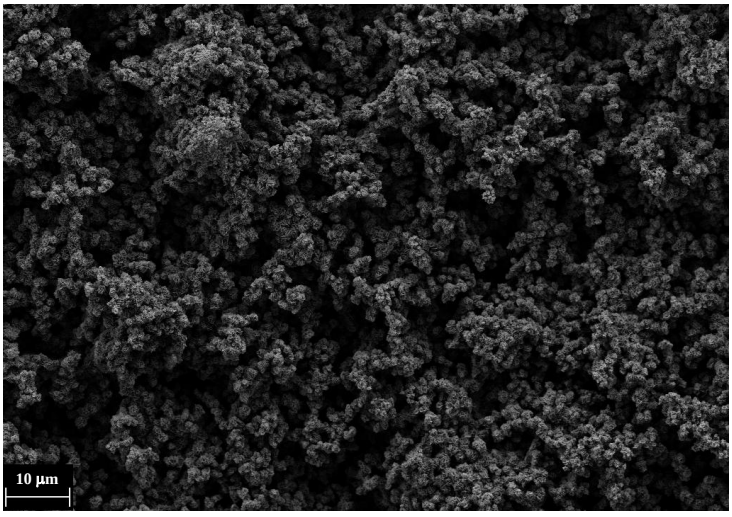

(c)

Figure 4

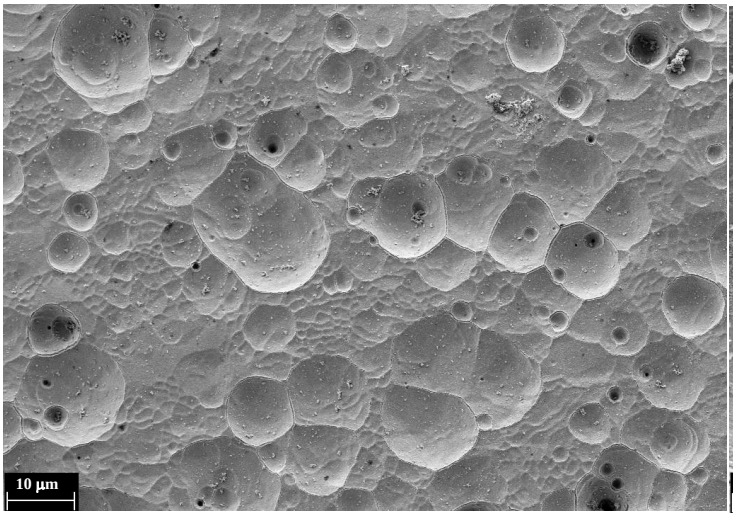

(a)

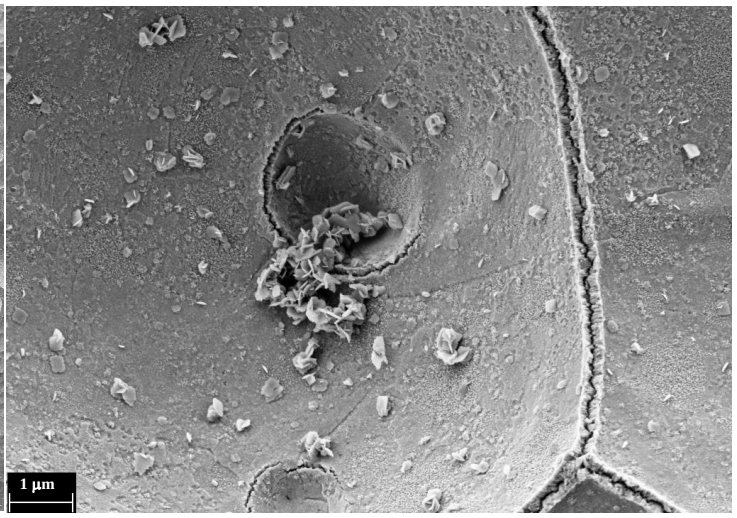

(b)

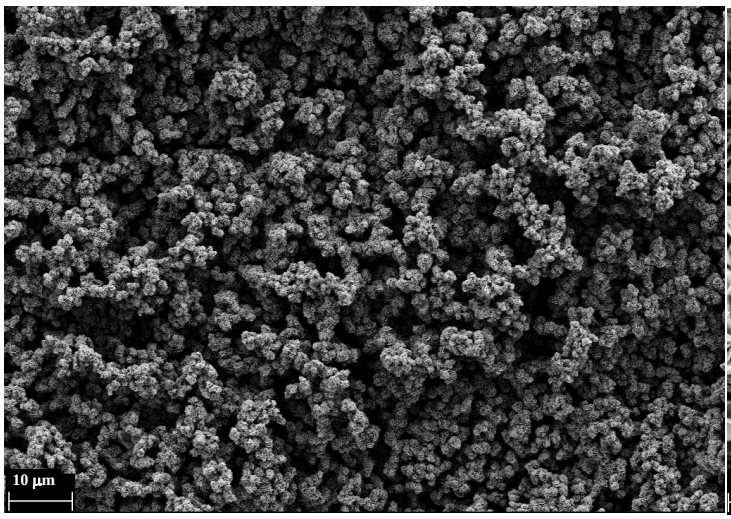

(c)

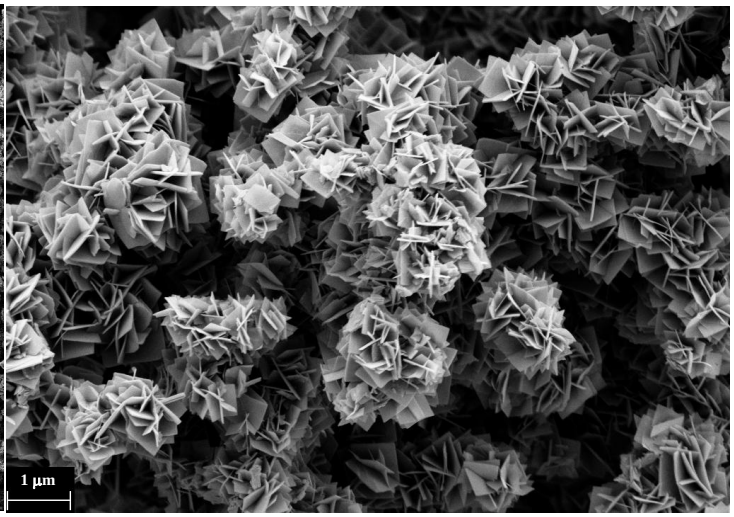

(d)

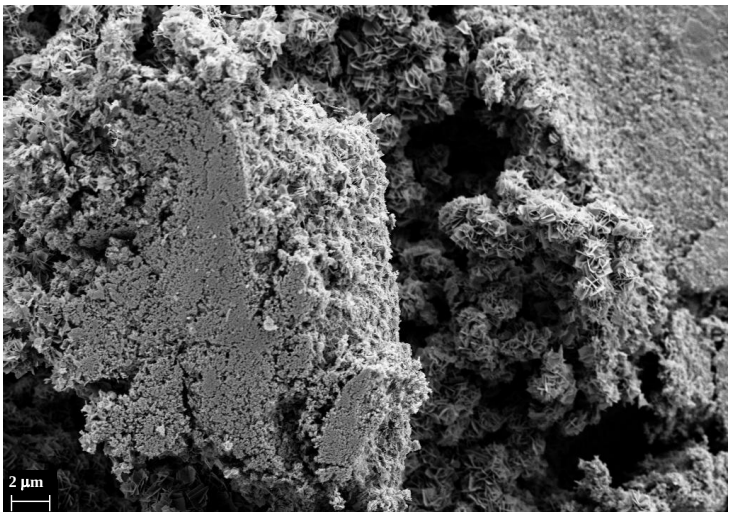

(e)

Figure 5

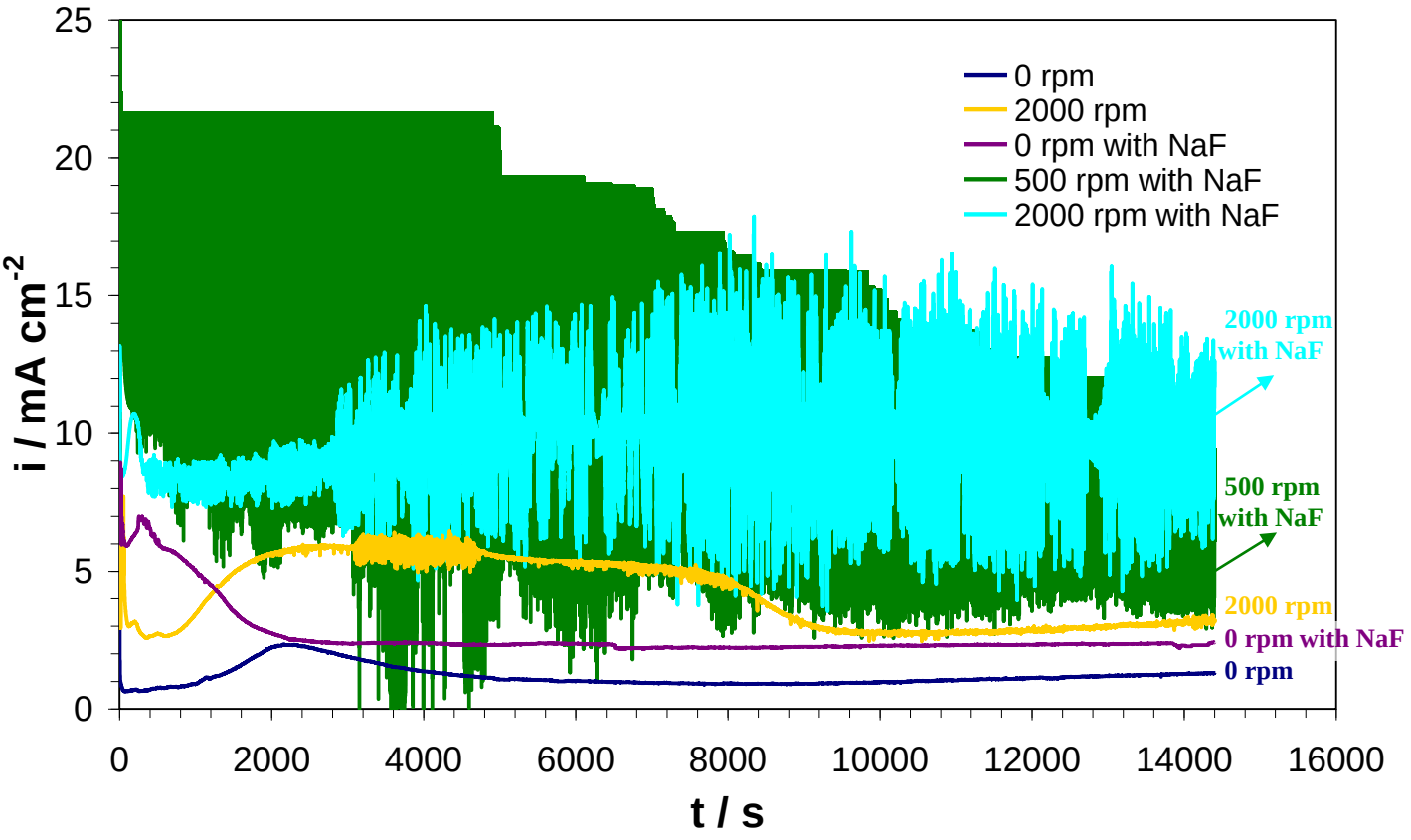
25
20
15
10
5
0
i / mA cm-2
0
2000
4000
6000
8000
10000
12000
14000
16000
t / s
0 rpm
2000 rpm
0 rpm with NaF
500 rpm with NaF
2000 rpm with NaF
2000 rpm with NaF
500 rpm with NaF
2000 rpm
0 rpm with NaF
0 rpm

Figure 6

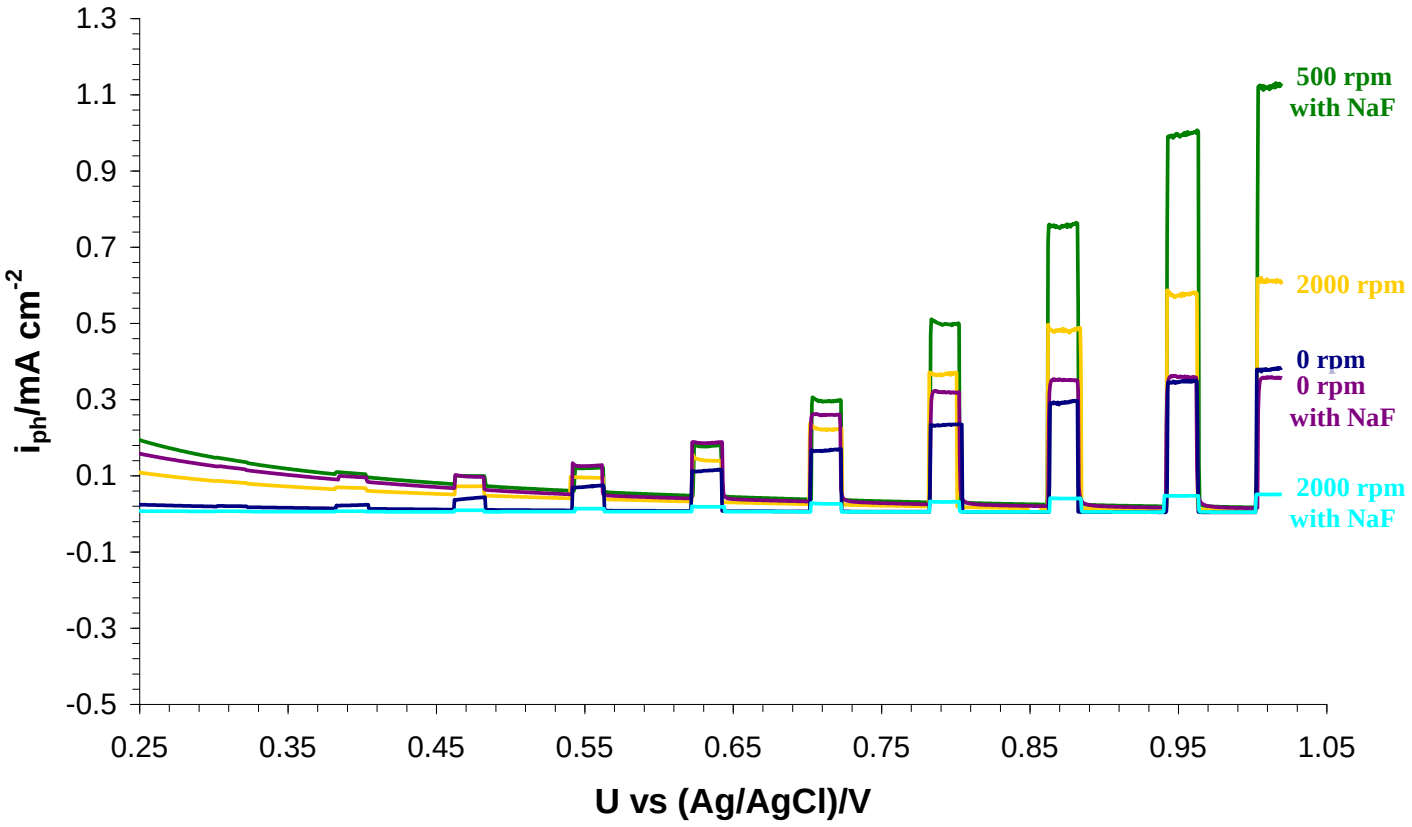
1.3
1.1
0.9
0.7
0.5
0.3
0.1
-0.1
-0.3
-0.5
i_{ph}/mA cm^{-2}
0.25
0.35
0.45
0.55
0.65
0.75
0.85
0.95
1.05
U vs (Ag/AgCl)/V
500 rpm with NaF
2000 rpm
0 rpm
0 rpm with NaF
2000 rpm with NaF